ACCOUNTS
of chemical research

The Valence Bond Way: Reactivity Patterns of Cytochrome P450 Enzymes and Synthetic Analogs

SASON SHAIK,* WENZHEN LAI, HUI CHEN, AND YONG WANG

Institute of Chemistry and the Lise-Meitner-Minerva Center for Computational Quantum Chemistry, The Hebrew University of Jerusalem, 91904 Jerusalem, Israel

RECEIVED ON MARCH 4, 2010

CONSPECTUS

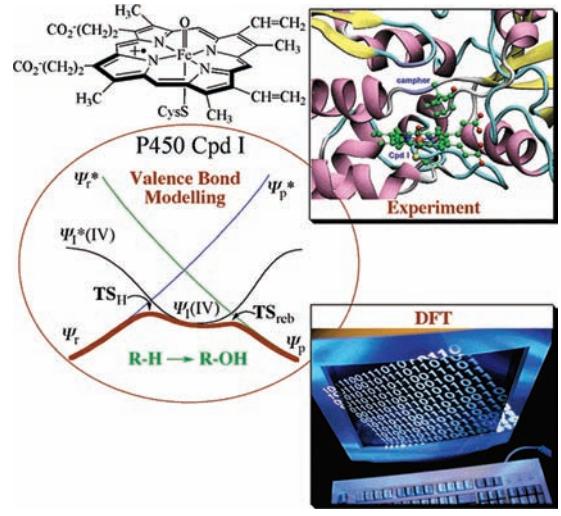

The preceding decade has witnessed an immense surge of activity in the bioinorganic chemistry of transition metal enzymes and synthetic analogs that model their operation. The wide range of research covers both experimental and theoretical investigations of structure and reactivity patterns. Theory, and especially density functional theory (DFT), has become a very useful tool, an important partner of experiment in resolving structural and mechanistic issues. This flare of activity has generated a great deal of knowledge on intermediates, transition states, barriers, rate constants, rate−equilibrium relationships, stereoselectivity, and so forth.

This abundance of acquired knowledge has created the need for establishing order, namely, the outlining of broad generalizations, as well as the creation of a more-intuitive interface between experimental and theoretical data. The valence bond (VB) diagram model, originally developed for organic reactions, is such a theoretical framework that has the potential to guide the requisite generalizations in the field of bioinorganic chemical reactivity. In this Account, we briefly describe the principles of construction of VB diagrams for bioinorganic reactions, detailing applications in the booming research area of heme enzyme (specifically cytochrome P450) reactivity, and particularly two archetypal reactions of these enzymes, alkane hydroxylation and thioether sulfoxidation. For congruence with the *lingua franca* of bioinorganic chemistry, the VB model is formulated to create bridges to (i) the molecular orbital (MO) description, (ii) the oxidation state formulation of transition metal complexes, and (iii) widely used concepts such as the Bell−Evans−Polanyi (BEP) principle.

The VB diagram model reveals the origins of the barrier, describes the formation of transition states and reaction intermediates, and allows the prediction of barrier heights and structure−reactivity relationships. Thus, from the VB diagram model, we can rationalize the mechanistic selection during alkane hydroxylation compared with thioether sulfoxidation, as well as the different behaviors of the spin states during the reactions with the active species of P450, the high-valent iron oxo species called compound I (Cpd I). Furthermore, the VB model leads to expressions that enable us to estimate barrier heights from easily accessible reactant properties, such as bond energies, ionization potential, and electron affinities.

We further show that the model is not limited to these archetypal processes: its applicability is wider and more general. Accordingly, we outline the potential applications of these principles to other reactions of P450 (such as olefin epoxidation and arene hydroxylation) and to similar reactions of nonheme enzymes and synthetic models. The VB diagram model leads to a unified understanding of complex bioinorganic transformations, creates order in the data, and provides an important framework for making useful predictions.

Published on the Web 06/07/2010 www.pubs.acs.org/acr
10.1021/ar100038u

Introduction

P450s are hemoproteins that metabolize and biosynthesize essential compounds[1] by use of a high-valent iron−oxo porphyrin cation-radical complex, Por$^{+\bullet}$Fe(IV)O, so-called compound I (Cpd I), shown in Scheme 1 along with some oxo-transfer reactions it performs.

Thus, Cpd I is a "dream reagent" that can perform many different reactions.[1] However, this reagent has generated also rich reactivity patterns.[1b,c,2,3] Some of this richness derives from the electronic structure of Cpd I,[1b,c,2] which possesses two closely lying spin states, a high-spin (HS) quartet state and a low-spin (LS) doublet state.[2] As such, the ground state of Cpd I is triradicaloid, prone to initiate radical-type reactions, which involve competing reactions of the two spin states, referred to as two-state reactivity (TSR).[2,4] A typical TSR is alkane hydroxylation, which transpires via the stepwise HS mechanism and an effectively concerted LS mechanism illustrated in Figure 1a.[2,4b] By contrast, thioether sulfoxidations proceed by concerted mechanisms generally with a large LS preference, as shown in Figure 1b.[5,6] What is the root cause for these mechanistic choices is a question we intend to answer herein.

Additionally, being electron-deficient, Cpd I is prone to undergo electrophilic-type reactions.[1a−c,2,3] For example, the rates of sulfoxidation correlate with the thioethers' oxidation potentials.[7,8] In other cases, like arene hydroxylation, the species along the reaction coordinate possess hybrid radical/cation characters.[2a,9] Topping these features is the fact that Cpd I undergoes "two-electron reduction", and hence it generates intermediate electromers, for example, PorFe(IV)OH/R$^{\bullet}$ and Por$^{+\bullet}$Fe(III)OH/R$^{\bullet}$ (Figure 1a), en-route to product.[2a] Altogether, these features make the reactivity of Cpd I extremely versatile, with multistate reactivity (MSR) scenarios,[2a,4b] *whereby radicals, cations, and cation radicals, on different spin manifolds, may all play a role in a single transformation that can either be stepwise (Figure 1*a) *or concerted (Figure 1*b). It is this kind of complexity that we wish to elucidate using the valence bond (VB) diagram model,[10−12] which until recently[5,13−16] dealt exclusively with organic reactions.

To derive general principles, we treat the processes in Figure 1 as archetypes of the reactions in Scheme 1 and deduce from first-principles the mechanistic choices, the spin-selection patterns, the alkane-hydroxylation reactivity dependence on C−H bond energies[1d] compared with on oxidation potentials for sulfoxidation, and the dependence of reactivity on the axial ligand of Cpd I in synthetic models.[16]

SCHEME 1

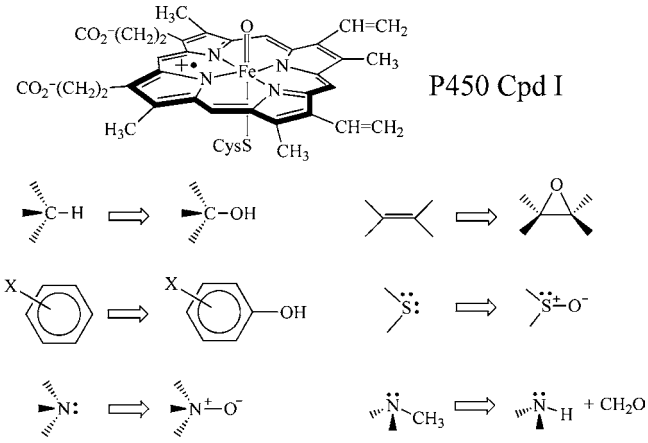

Bridges

We begin with bridges between the VB language and the *lingua franca* of bioinorganic chemistry.[5,14]

Oxidation States. This formalism tracks d-electron counts of transition-metal complexes during redox processes. We discuss three examples, because later we shall illustrate how this electron-counting mode is embedded in the VB model.

Scheme 2a shows oxidation numbers for Cpd I: the porphyrin has a σ-oxidation number of 2−, the oxo is 2−, and the thiolate is 1−. Since the molecule is neutral, the heme oxidation state is V, which becomes Por$^{+\bullet}$Fe(IV)O, based on spectroscopic evidence[1c−e] for a porphyrin π-cation radical. With Fe(IV), Cpd I will have a d^4 electronic configuration, in accord with all evidence.[1b−e,2,6,9]

Scheme 2b depicts the iron-hydroxo electromers due to H-abstraction by Cpd I. The resulting OH group has an oxidation number of 1−, and hence the effective oxidation state of the heme becomes IV. This can manifest as PorFe(IV)OH or Por$^{+\bullet}$Fe(III)OH, with electronic configurations d^4 and d^5, respectively.

MO−VB Bridges. Figure 2a shows key MOs of Cpd I: The $\sigma_{FeO}^2\pi_{FeO}^4\pi^*_{FeO}{}^2$ configuration represents the bonding block and accounts for a σ-FeO bond and a $\pi_{FeO}^4\pi^*_{FeO}{}^2$ manifold, as in $^3O_2$,[2a,4,5,14,17,18] having a bond order 2 and spin-up electrons in π^*_{FeO}. These π^* orbitals are considered also as "d" orbitals, so that the d-block occupancy is $\delta^2\pi^{*1}\pi^{*1}\sigma^*_{xy}{}^0\sigma^*_{z^2}{}^0$. Finally, the porphyrin cation-radical is represented by the singly occupied a_{2u}; the double-headed arrow represents spin-up or spin-down.

Figure 2b outlines the correspondence of the MO and VB representations of Cpd I, with the $\delta^2\sigma^*_{xy}{}^0\sigma^*_{z^2}{}^0$ block placed in parentheses. On the left, we show the bonding-block MO configuration, $\sigma_{FeO}^2\pi_{FeO}^4\pi^*_{FeO}{}^2$. In the VB representation, σ_{FeO} is drawn as a line, while the π-block is VB-represented by two

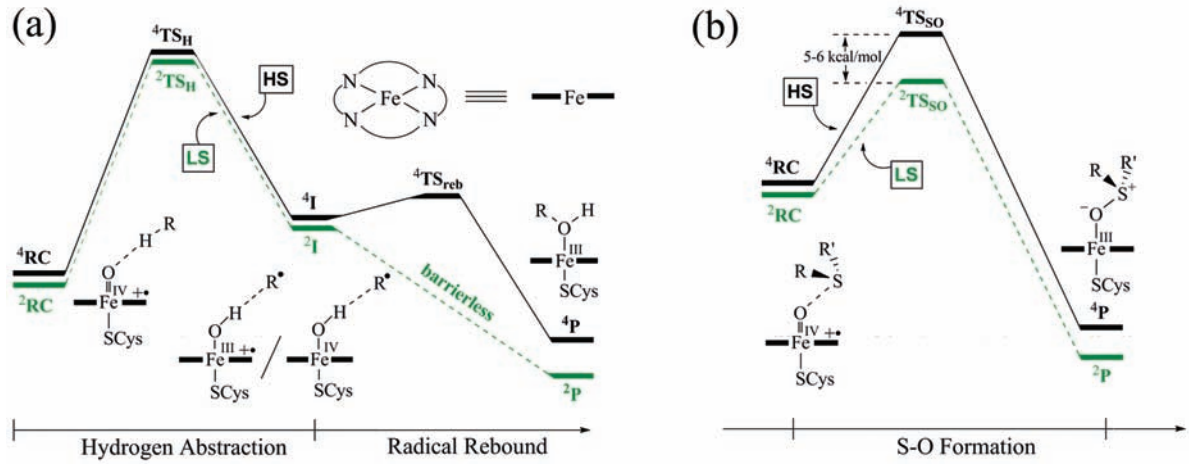

FIGURE 1. (a) Stepwise TSR in alkane hydroxylation and (b) concerted sulfoxidation.

SCHEME 2

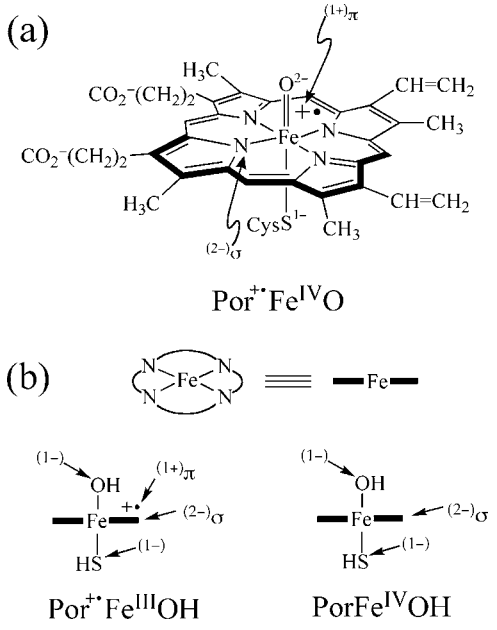

resonating three-electron bonds, which span two perpendicular planes, with two spin-up electrons on iron-oxo.[5,14,17,18] Finally, the open-shell a_{2u}^1 is represented by a cation-radical symbol on porphyrin. These VB cartoons will be used hereafter.

The reader may note that each of the resonance structures in Figure 2b looks like Fe^{III}—O$^{\bullet}$. Nevertheless, because their superposition relays four of the electrons to π_{FeO}-bonding orbitals, this leaves an Fe(d^4) configuration that qualifies as Fe^{IV}O. However, during the reaction the electronic structure gets localized and becomes Fe^{III}—O$^{\bullet}$.

VB Modeling of Archetypal Processes

To understand reactivity patterns, we need a model that shows how reactants evolve to products, the manners

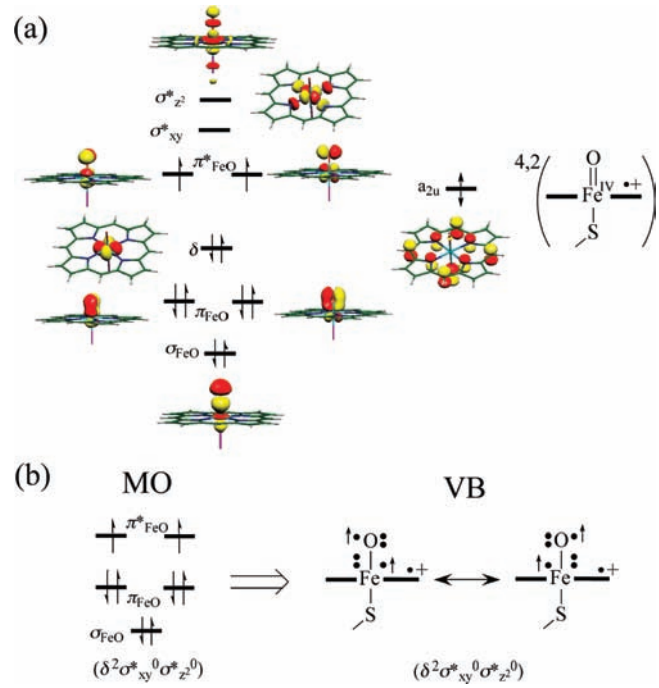

FIGURE 2. Cpd I: (a) MO representation; (b) MO—VB correspondence.

whereby the transition states (TSs) are generated, and the factors that determine barrier heights. This insight is achieved by the VB diagram model,[10–12] which, for any elementary step, involves two principal curves anchored at the ground states of reactants and products (Ψ_r, Ψ_p) and their two excited/promoted states (Ψ_p^*, Ψ_r^*), which are "electronic images" of the respective ground states with which they correlate. The correlation is based on the electron-pairing and oxidation-state identities between an "image state" in one end and the ground state in the other. The intersecting VB state curves mix, avoid the crossing, and generate thereby the **TS** and the barrier for the reaction. Such a generic diagram is Figure 3.

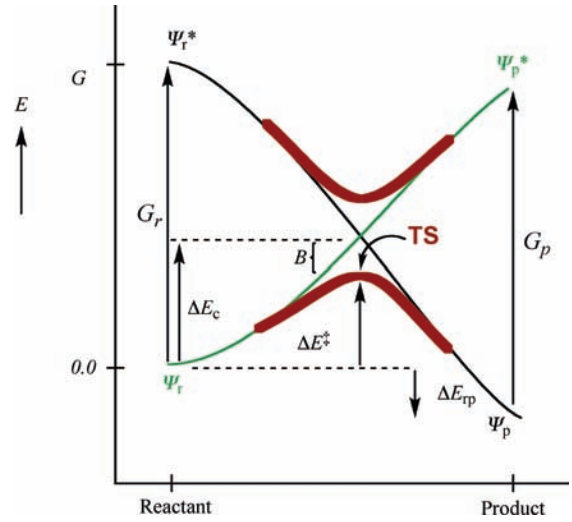

FIGURE 3. VB diagram describing the barrier ($\Delta E^{\ddagger}$) formation in an elementary step. *G*'s are promotion energies, *B* is the resonance energy of the TS, and ΔE_{rp} is the reaction energy. Here and elsewhere, the bold curve describes the result of VB mixing and avoided crossing.[10–12]

Alkane Hydroxylation

Figure 4 shows the VB diagram for alkane hydroxylation.[5,14] It involves two principal curves, anchored at the ground states (Ψ_r, Ψ_p) and their two promoted states (Ψ_p*, Ψ_r*), for the direct O-transfer to R−H. This process is, however, catalyzed by an intermediate-state curve (Ψ_I) that cuts through the higher-energy ridge for direct oxo transfer and splits the process into H-abstraction followed by radical rebound to form the ferric alcohol product. In the present forms, the diagrams show no spin-state information, which becomes indispensable only during rebound, and therefore, we put a question mark near the rebound transition state species, **TS**$_{reb}$.

Ψ_r describes R−H beside the VB-represented Cpd I.[5,14] In Ψ_r*, R−H donates one electron to porphyrin$^{+\bullet}$, and the H$^{\bullet}$ establishes an O$^{\bullet}$—$^{\bullet}$H bond-pair with the oxo of Cpd I. As argued for Scheme 2b, O$^{\bullet}$—$^{\bullet}$H localizes Cpd I to Fe^{III}—O$^{\bullet}$ and has an oxidation number −1. Since the oxo in Ψ_r is O^{2-}, consequently, in Ψ_r* the iron center gains an electron (from O^{2-}) and becomes Fe^{III}, as indicated in the cartoon near Ψ_r*. Taken together, Ψ_r* involves formal "two-electron reduction" of the heme, as in the final product, Ψ_p. These features and the R−O bond formation during rebound make Ψ_r* an "electronic image" of the product Ψ_p, and hence Ψ_r* is stabilized along the reaction coordinate and correlates to Ψ_p. Similar considerations apply to the correlation of Ψ_p* to Ψ_r.

The intermediate−VB curve, anchored in Ψ_I*, participates in the H-abstraction step. In Figure 4a, Ψ_I*(IV) involves an electron shift from iron to porphyrin$^{+\bullet}$. In addition, there is triplet unpairing of the C−H bond, while H$^{\bullet}$ and $^{\bullet}$O are coupled into a bond pair, which eventually becomes the O−H bond in Por-Fe^{IV}OH/R$^{\bullet}$. On the product side, Ψ_I*(IV) correlates to an excited state of the product having Fe(IV) and three electrons in the R···O linkage. The intermediate curve in Figure 4b is anchored in Ψ_I*(III), which involves C−H triplet unpairing. Thus, in both diagrams, the mixing of the three curves leads to a biphasic energy profile, a H-abstraction phase followed by radical rebound.

This is the place to comment about spin-state differences using $^2\Psi_r$* and $^4\Psi_r$* in Scheme 3. Thus, in both states we have

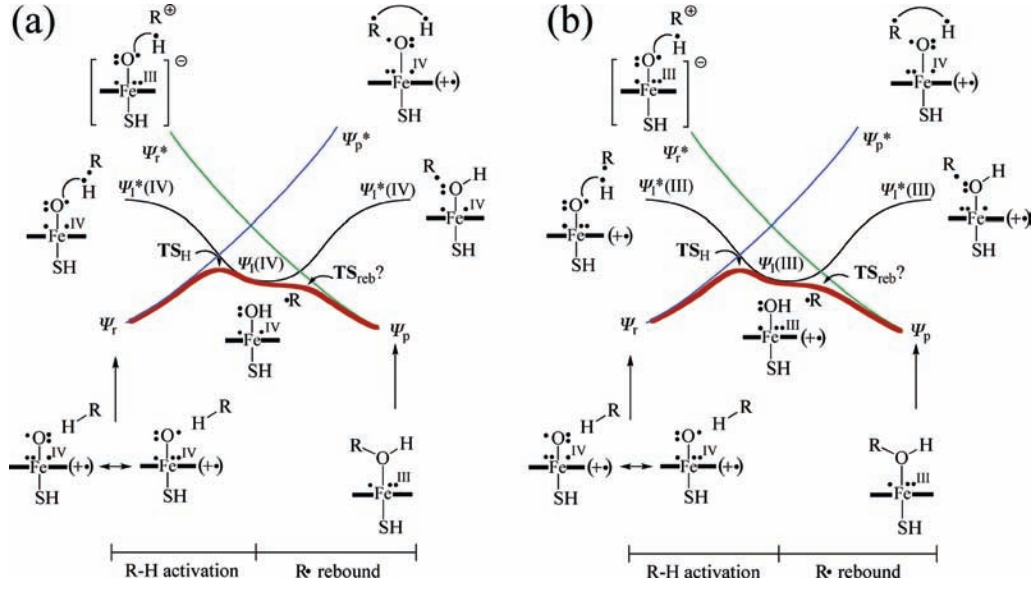

FIGURE 4. VB diagrams describing mechanistic scenarios during alkane (R−H) hydroxylation with intermediacy of (a) PorFe(IV)OH/R$^{\bullet}$, and (b) Por$^{+\bullet}$Fe(III)OH/R$^{\bullet}$. The covalent component of Ψ_r* is not shown.

SCHEME 3

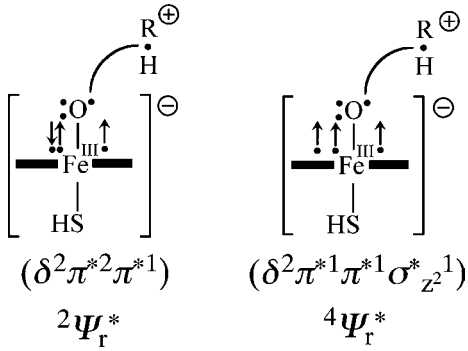

a PorFe(III)O•—•HR$^+$ species, which arises by electron transfer from the alkane to porphyrin$^{+\bullet}$, while coupling O• and •H to a bond pair. However, whereas the PorFe(III) moiety of $^2\Psi_r^*$ has a $\delta^2\pi^{*2}\pi^{*1}$ d-block configuration, $^4\Psi_r^*$ is typified by $\delta^2\pi^{*1}\pi^{*1}\sigma^*_{z^2}{}^1$. Thus, $^4\Psi_r^*$ involves also a $\pi^* \rightarrow \sigma^*_{z^2}$ promotion within the d-block. The $^4\Psi_p^*/^2\Psi_p^*$ difference is simply in the spin direction of the porphyrin cation radical. Since the VB crossing during the H-abstraction phase does not involve the $^{2,4}\Psi_r^*$ states, the spin-state profiles remain close in energy during H-abstraction,[14] and the spin-preference appears primarily during rebound where the state crossing involves $^{4,2}\Psi_r^*$.

Radical Rebound. The rebounds start from the midpoints of Figures 4a,b and convert the iron-hydroxo/radical intermediates to ferric alcohols. The corresponding diagrams for the LS and HS rebounds of PorFe(IV)OH/R• are shown in Figure 5.[14] To underscore the spin-state differences, the VB cartoons come here with MO diagrams, revealing occupancy changes in the d-type orbitals during rebound.

In Figure 5a, $^2\Psi_r^*$ is ^{2}[PorFe(III)OH$^-$/R$^+$] due to one electron transfer from the radical (R•) in the ground state to the d(π^*) orbital of the PorFe(IV)OH species. Along the C—O bond-formation coordinate, $^2\Psi_r^*$ correlates to the ground state of the ferric alcohol complex ($^2\Psi_p$), while $^2\Psi_I$(IV) rises to become an excited state $^2\Psi_I^*$(IV). Similarly, $^4\Psi_r^*$ (Figure 4b) involves electron transfer from R• to d($\sigma^*_{z^2}$), forming ^{4}[PorFe(III)OH$^-$/R$^+$], which correlates to the ferric alcohol complex ($^4\Psi_p$). The VB mixing of the corresponding state curves generates the LS/HS-rebound energy profiles.

The reason for the spin-state selectivity during rebound originates in the respective promotion-energy gaps in Figure 5. Thus, G_{HS} is larger than G_{LS} by an orbital-excitation energy term, which is significant. As such, the HS rebound will have a barrier, while the LS process would be barrier-free.[13,14] Analogous diagrams will correspond to Por$^{+\bullet}$Fe(III)OH/R•. However, here the $^4\Psi_r^*$ state is generated by one-electron transfer from R• to d($\sigma^*_{z^2}$), while another electron shifts from d(π^*) to the porphyrin-hole orbital, therefore resulting in poor VB mixing[4b,12] and a higher barrier compared with the ^{4}PorFe(IV)/R• electromer.

In summary, the VB model shows that LS alkane hydroxylation is effectively concerted with a barrier-free rebound while HS hydroxylation is stepwise. Furthermore, since the promotion gap for rebound is much smaller than for H-abstraction (see later), the rebound barriers are small compared with the H-abstraction barriers. Thus, the VB diagram retrieves the mechanistic scenario[2a] of alkane hydroxylation (Figure 1a).

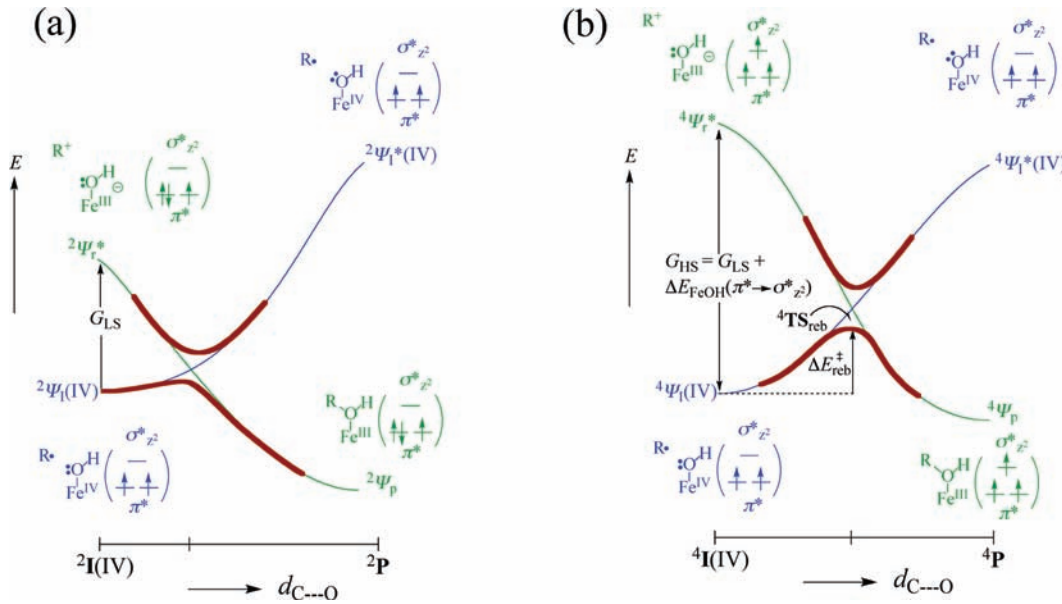

FIGURE 5. VB diagrams describing the rebound energy profiles for (a) ^{2}[PorFe(IV)OH/R•] and (b) ^{4}[PorFe(IV)OH/R•].

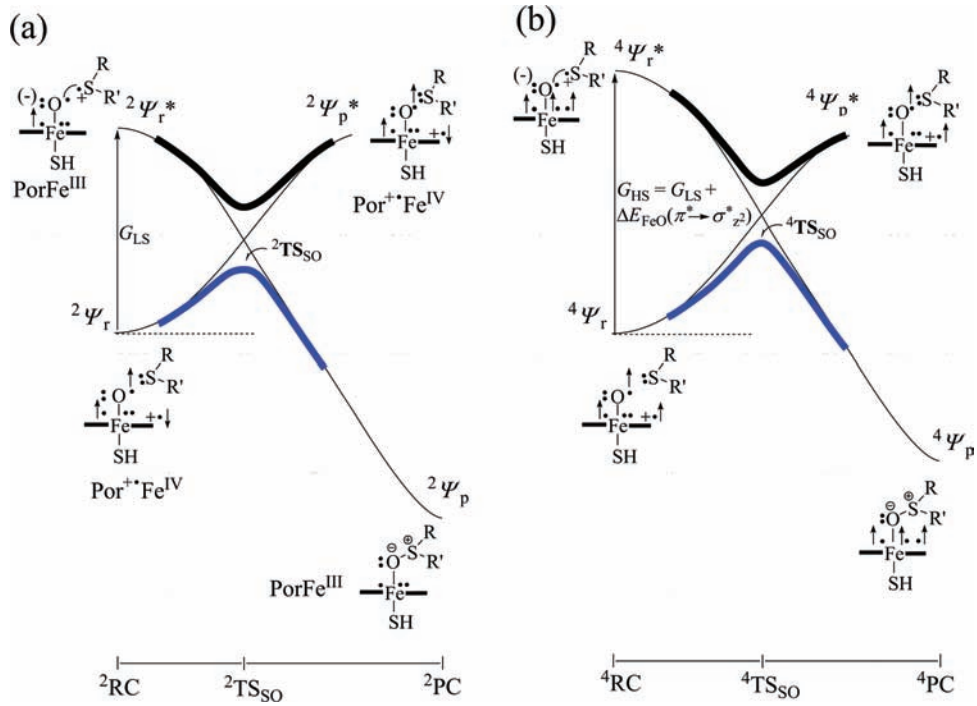

FIGURE 6. VB diagrams for sulfoxidation by Cpd I in the (a) doublet and (b) quartet states. For simplicity, Cpd I is represented by one VB structure.

VB Modeling of Sulfoxidation

The mechanistic scenario of alkane hydroxylation is dominated by the intermediate state curve (Figure 4). In sulfoxidation, however, there is no such low-lying intermediate state, and therefore the process involves VB mixing of just the two principal curves, resulting in a direct oxo transfer, as shown in Figure 6.

The promoted states are similar to those discussed for alkane hydroxylation. For example, $^2\Psi_r^*$ in Figure 6a involves one electron transfer from the sulfur lone pair to porphyrin$^{+\bullet}$, while coupling $S^{\bullet+}$ and $O^\bullet$ into a bond pair ($O^\bullet—{}^\bullet S^+$). This coupling modifies the oxidation number of the oxo to 1−, thus reducing the iron oxidation state to Fe^{III}. As such, $^2\Psi_r^*$ and $^2\Psi_p$ have identical bond-pairing and oxidation numbers, and hence, the two states correlate along the reaction coordinate. The VB diagram for the quartet-state process (Figure 6b) is similar, with the exception that $^4\Psi_r^*$ involves also a promotion of an electron within the d-block from the π^* orbital to $\sigma^*_{z^2}$.[5] Thus, sulfoxidation involves synchronous electron transfer and O···S bond making; the quartet process involves also simultaneous promotion within the d-block.

Reactivity Patterns

Based on Figure 3, the simplest expression for the barrier of an elementary step is eq 1:

$$\Delta E^{\ddagger} = fG_r - B \qquad (1)$$

Here the height of the crossing point (ΔE_c) is expressed as a fraction (f) of the promotion energy at the reactant side (G_r), and B is TS resonance energy.

Another expression is eq 2, which makes explicit the effects of the two promotion gaps and f factors using average quantities, and the contribution of the thermodynamic driving force, ΔE_{rp}:[12,19]

$$\Delta E^{\ddagger} \approx f_0 G_0 + 0.5\Delta E_{rp} + 0.5\Delta E_{rp}{}^2/G_0 - B;$$
$$G_0 = {}^1/_2(G_r + G_p), \quad f_0 = {}^1/_2(f_r + f_p) \qquad (2)$$

When an intrinsic contribution is defined as $\Delta E^{\ddagger}_{int} \approx f_0 G_0 - B$, eq 2 becomes[19]

$$\Delta E^{\ddagger} \approx \Delta E^{\ddagger}_{int} + 0.5\Delta E_{rp} + 0.5\Delta E_{rp}{}^2/G_0 \qquad (3)$$

This is similar to the Marcus equation, while providing an explicit expression for $\Delta E^{\ddagger}_{int}$. The thermodynamic driving force in eqs 2 and 3 embodies the rate-equilibrium relationship known as the Bell−Evans−Polanyi (BEP) principle.[20] In eq 1, the BEP effect is implicit in the f factor, which varies with reaction exothermicity.[11,12]

Alkane Hydroxylation

H-Abstraction. Equation 1 is designed for "reaction families", wherein f and B are quasi-constant.[11,12] The promotion energy for H-abstraction (G_H) is the gap from the reactant state Ψ_r to Ψ_I^*(IV) in Figure 4a. For both spin manifolds, G_H involves

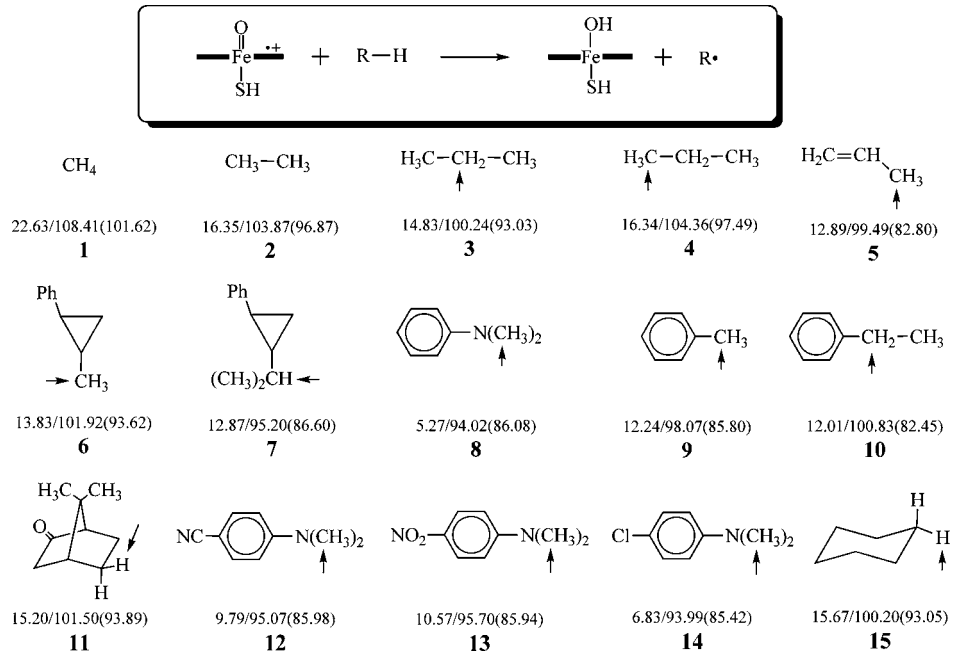

FIGURE 7. Alkanes **1**−**15** and computed DFT data (in kcal/mol), shown as $\Delta E^{\ddagger}_{av}/D_{CH}(BDE_{CH})$. $\Delta E^{\ddagger}_{av}$ are spin-state averaged barriers, here and elsewhere calculated with a triple-ζ polarized basis-set with ZPE correction.

decoupling of the C−H bonding electrons into a triplet,[19,21] which can be expressed as in eq 4:

$$G_H \approx 2D_{CH} = 2(BDE_{CH} + |RE_{R\bullet}|) \quad (4)$$

Here $RE_{R\bullet}$ is the relaxation energy of the radical $R^{\bullet}$; hence, D_{CH} is a vertical bond-dissociation energy.[14,22a,b]

The resonance energy of the TS in H-abstraction processes was previously derived as[14,19]

$$B \approx {}^1/_2(BDE_W) \quad (5)$$

BDE_W is the bond dissociation energy of the weaker of the two bonds (C−H/FeO−H) that are broken and formed during the reaction. For Cpd I and the range of alkanes whose reactivity we wish to model, these *B* values range between 41 and 45 kcal/mol. Finally, the factor *f* was theoretically derived to be $^1/_3$.[14,19]

To *avoid individual parameters for each reaction*, we seek common *f* and *B* that are close to the above theoretical values and that can account for the general pattern of the DFT barriers for H-abstraction, albeit less accurately than having "precise individual parameters". As we showed,[14] H-abstraction reactions behaved as a "reaction family" and their barriers could be estimated by the following expression, with *f* and *B* being close to the expected values from theoretical analyses:[19]

$$\Delta E^{\ddagger}_{VB} = 0.6D_{CH} - 46.78\ (\text{kcal/mol}); \quad G_H = 2D_{CH} \quad (6)$$

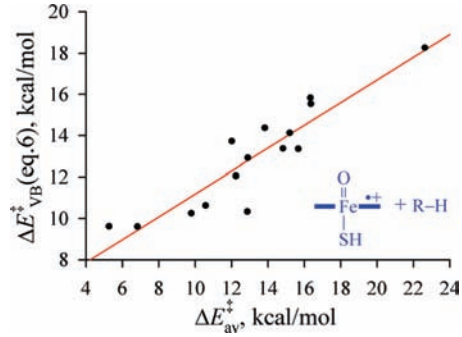

FIGURE 8. VB barriers (eq 6) plotted against averaged DFT barriers.

To demonstrate its utility, we applied eq 6, as is, to estimate barriers for the alkanes in Figure 7, which were studied in our group.[14,16,22a,c] The entire data set has $R^2 = 0.833$ (see also Figure S1, Supporting Information). More importantly, excluding **1**, **8**, and **14**, which deviate the most from the DFT barriers, produces a set of VB barriers with a mean deviation of ±0.90 kcal/mol compared with DFT (Figure 8). As such, eq 6 appears to predict quite well the computed barriers, and the series behave as "a reaction family" with small scatters in the *f* and *B* quantities.

It is instructive to consider some of the most-deviant cases in the light of the VB model. H-abstraction from methane (**1**) is the most endothermic in the series, which means that a larger *f* value ($f > 0.3$) would have been required to reproduce this barrier.[11,12]

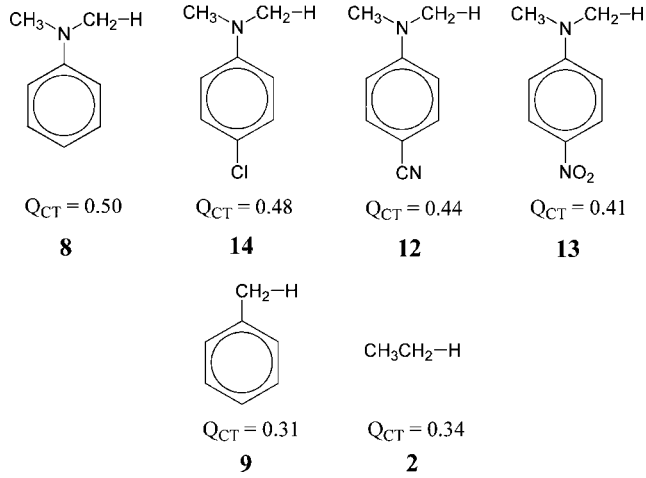

FIGURE 9. Charge transfer values (Q_{CT}) from alkanes to Cpd I in the corresponding $\mathbf{TS}_H$ species.

For *N*,*N*-dimethylaniline (DMA, **8**), eq 6 predicts a barrier of 9.63 kcal/mol, while the DFT barrier is 5.27 kcal/mol. By contrast, eq 6 predicts well the barriers for the *para*-CN- and *para*-NO_2-substituted DMAs (**12**, **13**) and for toluene (**9**), all having similar BDE_{CH}'s to DMA.[22c] DMA (**8**) has a low ionization potential, and hence, its charge-transfer state (Ψ_r^* in Figure 4a) is low-lying and close to the intermediate state curve, which is responsible for H-abstraction. *Consequently,*[10–12] *the charge-transfer state mixes strongly into* $\mathbf{TS}_H$(**8**) *and induces a strong polar effect in the H-abstraction process*.

There are a few probes that reveal this mixing,[2a,14] one of them is the charge transfer (Q_{CT}) from the alkane to Cpd I in the $\mathbf{TS}_H$. Comparison of the NBO-computed values in Figure 9 reveals that DMA (**8**) transfers the largest amount of charge compared with other substrates. Such a Q_{CT} value reveals the expected strong mixing of the charge-transfer state into the $\mathbf{TS}_H$ species, due to the conjugation of the nitrogen lone-pair of **8** into the cationic center.[2a,14] This mixing is weaker for the *p*-CN and *p*-NO_2 DMAs (**12**, **13**), and absent for toluene (**9**) and ethane (**2**). Thus, the deviation of **8** from the barrier predicted by eq 6 is caused by the larger resonance energy factor, *B* (51.14 vs 46.78 kcal/mol), which reflects stronger VB mixing in the corresponding $\mathbf{TS}_H$ species. An augmented *B* applies also to the deviation of **14** ($B = 49.65$ vs 46.78 kcal/mol).

Let us emphasize in summary that our goal here was to model the DFT barriers,[14,22] which exhibit trends qualitatively similar to relative reactivity deduced from experiment[1c,d] using internally consistent D_{CH} values. It is entirely acceptable to use experimental BDE_{CH}'s with eqs 1 and 6, assuming that $RE_{R\bullet}$ values can also be extracted from experimental data, as done by Sanderson.[23] Thus, while eq 6 is clearly not a panacea, it is useful, and together with the VB diagram model, it provides insight into major factors that determine the barrier.

Radical Rebound. At the rebound junction (Figure 5), the promotion-energy gaps are rather small and given by eq 7a:

$$^2G_{reb} = IP_{R\bullet} - EA_{FeOH} - C \qquad (7a)$$

$$^4G_{reb} = IP_{R\bullet} - EA_{FeOH} - C + \Delta E_{FeOH}(\pi^* \rightarrow \sigma^*_{z^2}) \qquad (7b)$$

$IP_{R\bullet}$ is the radical-ionization potential, EA_{FeOH} is the electron affinity of the iron-hydroxo complex, *C* is the Coulomb stabilization energy in ^{4,2}[PorFe(III)OH^-/R^+], while $\Delta E_{FeOH}(\pi^* \rightarrow \sigma^*_{z^2})$ is the orbital-excitation term. This last term (26 kcal/mol) appears only for $^4G_{reb}$ and constitutes a large fraction of the total gap. Consequently, without this quantity, the doublet-state rebound would generally be barrier-free.

Using $^4G_{reb}$ with eq 1 for the barrier, we can outline rebound-reactivity scenarios. Thus, in a series of radicals with one iron-hydroxo complex, $^4G_{reb}$ is governed by changes in $IP_{R\bullet}$: the smaller the $IP_{R\bullet}$, the lower is the rebound barrier. This trend was discussed before[13] for a series of experimental systems including **6** and **7**.[1d,24] Thus, since $IP(\mathbf{6}_{R\bullet}) > IP(\mathbf{7}_{R\bullet})$ by ca. 11 kcal/mol,[13] **6** exhibits some radical-rearrangement products, while **7** shows none.[24,25] One can further predict that changes of cysteine to electron-withdrawing ligands (CF_3SO_3) will diminish the rebound barriers, since these changes increase EA_{FeOH} in eq 7b,[16] while decreasing $\Delta E_{FeOH}(\pi^* \rightarrow \sigma^*_{z^2})$ due to $\sigma^*_{z^2}$ orbital-energy lowering.[13] Finally, replacing iron by the stronger-binding ruthenium will increase the corresponding $\Delta E_{RuOH}(\pi^* \rightarrow \sigma^*_{z^2})$ quantity and lead to a large rebound barrier.[26] A similar rationale predicts[13] that different P450 isozymes will possess different rebound barriers and exhibit thereby variable extents of radical-rearranged products.

Reactivity Patterns in Sulfoxidation

Sulfoxidation by Cpd I exhibits reactivity reminiscent of single-electron transfer (SET) reactions, but without traces of thioether cation radicals, thus implying a direct oxo-transfer mechanism with some SET character.[7,8] To probe these trends, we computed[5] P450 sulfoxidation of the *para*-substituted thioanisoles (SRR') in Scheme 4, which were reported to exhibit a correlation of rates with the thioanisole redox potentials.[7]

SCHEME 4

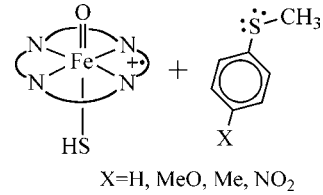

The DFT results[5,6a] revealed a concerted reaction (e.g., Figure 1b) with a lower LS surface[6b] and barriers that correlated[5] with the ionization potentials ($IP_{SRR'}$) and the oxidation potentials of the thioanisole. Figure 6 reveals that the reasons for these reactivity patterns derive from the promotion gaps, in eqs 8a and 8b, where $EA_{Cpd\ I}$ is the electron affinity of Cpd I:

$$G_{LS} = IP_{SRR'} - EA_{Cpd\ I} \quad (8a)$$

$$G_{HS} = IP_{SRR'} - EA_{Cpd\ I} + \Delta E_{FeO}(\pi^* \rightarrow \sigma^*_{z^2}) \quad (8b)$$

Application of the barrier expression in eq 1 shows[5] that the sulfoxidation of thianisoles behaves as a "reaction family", with constant $f = 0.2$ and $B = 13.5$ kcal/mol, which are theoretically acceptable values for reactions that involve synchronous SET and bond making.[27,28] The barrier expression is given by eq 9:

$$\Delta E^{\ddagger}_{VB} = 0.2G_{LS/HS} - 13.5\ \text{kcal/mol} \quad (9)$$

This magnitude of B rules out an outer-sphere SET, where $B \rightarrow 0$, since such a TS would have lost 13.5 kcal/mol of stabilization energy. This conclusion accords with the lack of thioether cation radicals in these reactions,[8] unless the reaction were done with enzymes that deny the thioanisole access to Cpd I.[29]

Figure 10 plots the predicted $\Delta E^{\ddagger}_{VB}$ against $\Delta E^{\ddagger}_{DFT}$ values for both HS and LS states ($R^2 = 0.984$). Furthermore, combining eqs 8a and 9 shows that the difference between the HS and LS barrier is given as follows:

$$\Delta E^{\ddagger}_{HS} - \Delta E^{\ddagger}_{LS} = 0.2\Delta E_{FeO}(\pi^* \rightarrow \sigma^*_{z^2}) \quad (10)$$

Using the calculated $\Delta E_{FeO}(\pi^* \rightarrow \sigma^*_{z^2})$ value predicts a barrier difference of 5.6 kcal/mol, in agreement with the DFT results.[5]

The BEP Principle

Since H-abstraction reactions[15,16,22,30–35] exhibit recurring correlations between rate constants and BDE_{CH} or BDE_{FeOH}, it is important to establish when such correlations reflect genuine BEP effects.[20] For a data set with various Cpd I's and alkanes,[14,16,36] the barrier expression eq 2, which treats symmetrically the reactant and product ends, allows an appreciation of the role of the reaction driving force. Figure 11 shows the VB diagram for H-abstraction, with promotion gaps noted at both sides.[19]

Neglecting the quadratic term, eq 2 can be rewritten as follows:[19]

$$\Delta E^{\ddagger}_{VB} \approx f_0[D_{CH} + D_{FeO-H}] + 0.5\Delta E_{rp} - B \quad (11)$$

D_{CH}/D_{FeO-H} are vertical bond energies at the diagram extremes (Figure 11). Although we know that with such a variety of alkanes **1**–**15** (Figure 7)[14,22a,c] and L–Cpd I species (**16**–**18**, Figure 11),[16] we cannot expect constant f_0 and B, still it is instructive to keep the same parameters as above, and use $f_0 = 0.3$ and $B = 46.78$ kcal/mol, to estimate all the corresponding barriers.[14,22a,c] Figure 12 shows these barriers plotted against DFT values. Considering the variety of reactions and the assumption of constant f_0 and B, the scatter is expectedly significant ($R^2 = 0.729$). Other modifications in eq 11 are

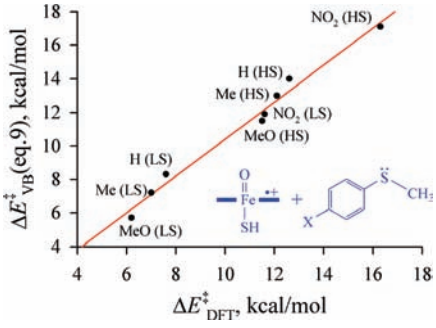

FIGURE 10. A plot of VB barriers (eq 9) vs DFT computed ones.[5]

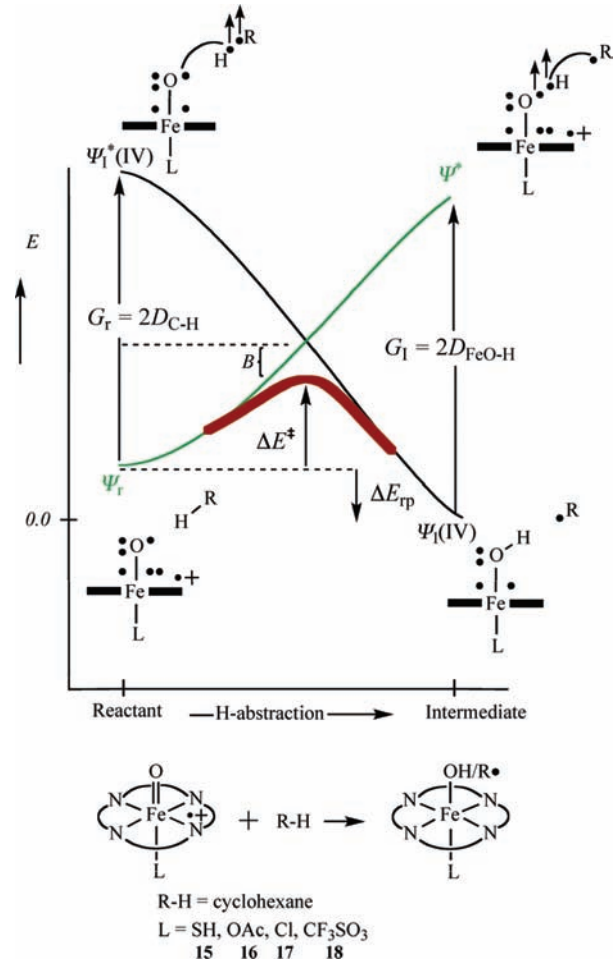

FIGURE 11. VB diagram for H-abstraction from alkanes by Cpd I species with variable ligands, L.

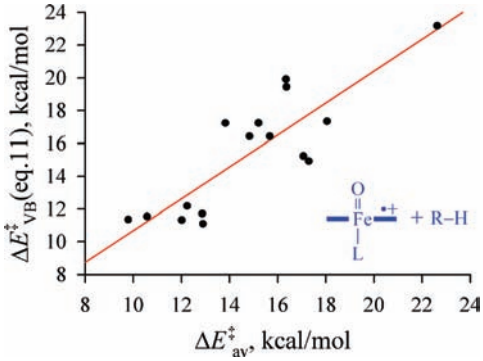

FIGURE 12. VB barriers (eq 11) plotted against DFT barriers.

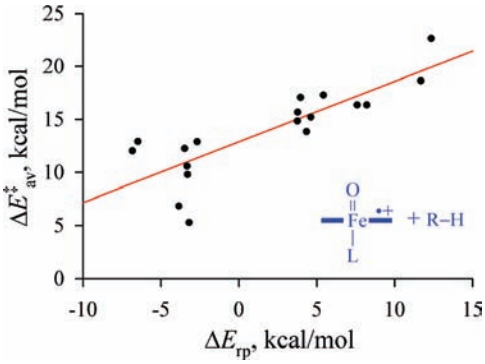

FIGURE 13. A BEP plot for **1**−**18**.

placed in the Supporting Information (Table S5), including a BDE-only version ($R^2 = 0.821$, Figure S2).

Equation 11 gives insight into reactivity as an interplay of an intrinsic contribution, $f_0[D_{CH} + D_{FeO\text{-}H}] - B$, and the thermodynamic contribution, $0.5\Delta E_{rp}$. Thus,[19] the barrier originates in the first term, while the BEP term ($0.5\Delta E_{rp}$) is a modulator. For the entire set, $f_0[D_{CH} + D_{FeO-H}] - B = 14.25 \pm 2.76$ kcal/mol, which is quasiconstant. If it were strictly a constant, then the thermodynamic driving force, eq 12, would have to be the sole modulator of the barrier variations:

$$\Delta E_{rp} = \mathrm{BDE}_{CH} - \mathrm{BDE}_{FeO-H} \qquad (12)$$

Figure 13 shows a BEP plot for the entire data set (**1**−**18**). While as expected, the scatter is significant ($R^2 = 0.680$), still the data exhibit a general follow-up of the BEP principle.[20]

Let us focus on a trend observed recently in synthetic Cpd I's.[16,34] When we use the Cpd I series in Figure 11 and abstract the equatorial H from cyclohexane,[16] the VB expression for the barrier becomes

$$\Delta E^{\ddagger}_{VB} \approx A - 0.5\mathrm{BDE}_{FeO-H}; \quad A = f_0G_0 - B + 0.5\mathrm{BDE}_{CH} \qquad (13)$$

Since A in this series is quasiconstant, the barrier is expected to decrease in the series as BDE_{FeO-H} becomes larger, as manifested in Figure 14 ($R^2 = 0.756$).[16,35]

Similarly, for a series of Cpd I species and a given thioether,[36] the corresponding reaction energy is eq 13, while the barrier is given by eq 15:

$$\Delta E_{rp} = \mathrm{BDE}_{Fe=O} - \mathrm{BDE}_{O-SRR'} \qquad (14)$$

$$\Delta E^{\ddagger}_{SO} \approx A + 0.5\mathrm{BDE}_{Fe=O}; \quad A = f_0G_0 - B - 0.5\mathrm{BDE}_{O-SRR'} \qquad (15)$$

Assuming quasi-constant A, the barrier should correlate with $\mathrm{BDE}_{Fe=O}$, as generally revealed by Figure 15 ($R^2 = 0.741$).

Inspection of Figures 14 and 15 reveals that the axial ligand L applies generally opposing effects on $\mathrm{BDE}_{Fe=O}$ and BDE_{FeO-H}. Thus, the powerful π-donor substituents weaken the Fe═O bond of Cpd I but strengthen the FeO−H bond. As such, in accord with observations,[16,34,35] electron donating axial ligands enhance the reactivity toward H-abstraction and direct oxo-transfer reactions. These are bona fide BEP effects, which carry over to other systems.[33,35] However, being a modulator, the BEP effect will breakdown whenever the principal factors, G or B, vary adversely.[11,12] Such cases are apparent in Figures 13−15. For example, in sulfoxidation a donor ligand raises G by lowering the $\mathrm{EA}_{Cpd\ I}$ value thus canceling the thermodynamic advantage (L = OAc vs SH, Figure 15). Other cases have been reported in H-abstraction by oxo-ruthenium nonheme reagents.[16]

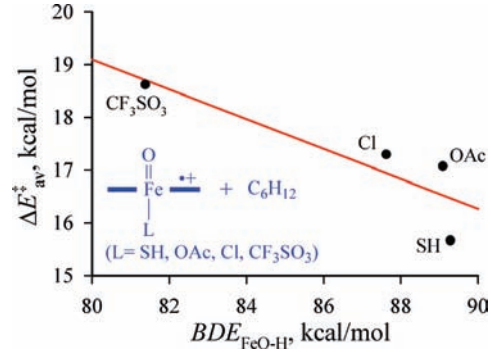

FIGURE 14. DFT barriers vs BDE_{FeO-H} for H-abstraction from cyclohexane.

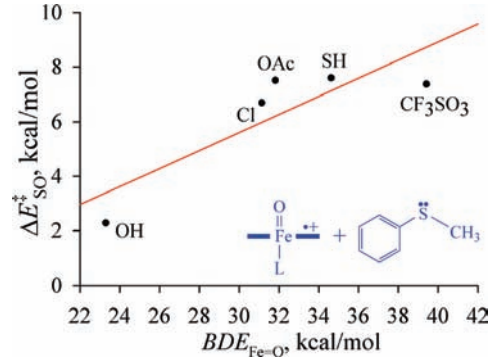

FIGURE 15. DFT barriers plotted against $\mathrm{BDE}_{Fe=O}$ for sulfoxidation of thianisole by L−Cpd I.

Prospects

Application of the VB diagram to archetypal reactions that are catalyzed by Cpd I of P450 leads to a unified understanding of complex bioinorganic transformations, creates order in the data, and lends itself to making predictions and interfacing between experimental and theoretical data.

The principles discussed herein can be generalized to other P450 processes. Thus, the sulfoxidation treatment is applicable to oxo-transfers to amines.[6a] Similarly, the alkane hydroxylation treatment is applicable to double-bond epoxidation and arene hydroxylation, with modifications: the intermediate state curves here involve triplet unpairing of the π-systems, and the charge-transfer state curves will be low-lying with significant mixing into the bond-activation TSs, *thereby leading to hybrid reactivity*.[9]

Nonheme reactivity[37] was shown[15] to follow similar lines. One challenge, however, is a first-principle derivation of the *enhanced reactivity* of higher spin-state reactions.[38,39] Still greater challenges will be met in the application of the VB model to P450 processes, which involve proton-coupled electron transfer, C−C bond coupling, etc.[2a]

Supporting Information Available. Methods of calculations, BDEs of FeO−H and Fe═O, activation energies for C−H cleavage of cyclohexane, results of DFT calculations, estimated f_0, B, and barriers by VB and DFT theories, and Cartesian coordinates of various ligand species. This material is available free of charge via the Internet at http://pubs.acs.org.

BIOGRAPHICAL INFORMATION

Sason Shaik is currently the Director of the Lise Meitner-Minerva Center at the Hebrew University. His major interests are in developing concepts for bonding and reactivity.

Wenzhen Lai is currently a postdoctoral associate of Sason Shaik and a former graduate of Nanjing University (2008). Her major interests are in heterogeneous and metallo-enzyme catalyses.

Hui Chen is currently a postdoctoral associate of Sason Shaik and a former graduate of Nanjing University (2006). His current major interest is in transition-metal chemistry.

Yong Wang is currently an associated professor at Dalian Institute of Chemical Physics (DICP). He was a former graduate of DICP (2007) and a postdoctoral associate of Sason Shaik.

FOOTNOTES

*To whom correspondence should be addressed: phone, +972-2-6585909; fax, +972-2-6584680/6585345; e-mail, sason@yfaat.ch.huji.ac.il.

REFERENCES

1 (a) *Cytochrome P450: Structure, Mechanism, and Biochemistry*, 4th ed.; Ortiz de Montellano, P. R., Ed.; Kluwer Academic/Plenum Publishers: New York, 2005. (b) Sono, M.; Roach, M. P.; Coulter, E. D.; Dawson, J. H. Heme-Containing Oxygenases. *Chem. Rev.* **1996**, *96*, 2841–2887. (c) Groves, J. In *Cytochrome P450: Structure, Mechanism, and Biochemistry*, 3rd ed.; Ortiz de Montellano, P. R., Ed.; Kluwer Academic/Plenum Publishers: New York, 2005; Chapter 1, pp 1−43. (d) Ortiz de Montellano, P. R. Hydrocarbon Hydroxylation by Cytochrome P450 Enzymes. *Chem. Rev.* **2010**, *110*, 932–948. (e) Denisov, I. G.; Makris, T. M.; Sligar, S. G.; Schlichting, I. Structure and Chemistry of Cytochrome P450. *Chem. Rev.* **2005**, *105*, 2253–2277.

2 (a) Shaik, S.; Cohen, S.; Wang, Y.; Chen, H.; Kumar, D.; Thiel, W. P450 Enzymes: Their Structure, Reactivity and Selectivity, Modeled by QM/MM Calculations. *Chem. Rev.* **2010**, *110*, 949–1017. (b) Yoshizawa, K. Theoretical Study on Kinetic Isotope Effects in C−H Bond Activation of Alkanes by Iron-Oxo Complexes. *Coord. Chem. Rev.* **2002**, *226*, 251–259.

3 Ortiz de Montellano, P. R.; De Voss, J. J. Oxidizing Species in the Mechanism of Cytochrome P450. *Nat. Prod. Rep.* **2002**, *19*, 477–493.

4 (a) Schröder, D.; Shaik, S.; Schwarz, H. Two-State Reactivity as a New Concept in Organometallic Chemistry. *Acc. Chem. Res.* **2000**, *33*, 139–145. (b) Shaik, S.; Hirao, H.; Kumar, D. Reactivity of High-Valent Iron Oxo Species in Enzymes and Synthetic Reagents: A Tale of Many States. *Acc. Chem. Res.* **2007**, *40*, 532–542. (c) Schwarz, H. On the Spin-Forbiddeness of Gas-Phase Ion−Molecule Reactions: Fruitful Intersection of Experimental and Computational Studies. *Int. J. Mass. Spectrom.* **2004**, *237*, 75–105.

5 Shaik, S.; Wang, Y.; Chen, H.; Song, J.; Meir, R. Valence Bond Modelling and Density Functional Theory Calculations of Reactivity and Mechanism of Cytochrome P450 Enzymes: Thioether Sulfoxidation. *Faraday Discuss.* **2010**, *145*, 49–70.

6 (a) Rydberg, P.; Ryde, U.; Olsen, L. Sulfoxide, Sulfur, and Nitrogen Oxidation and Dealkylation by Cytochrome P450. *J. Chem. Theory Comput.* **2008**, *4*, 1369–1377. (b) See however, HS preference in $P450_{BM3}$: Porro, C. S.; Sutcliffe, M. J.; de Visser, S. P. Quantum Mechanics/Molecular Mechanics Studies on the Sulfoxidation of Dimethyl Sulfide by Compound I and Compound 0 of Cytochrome P450: Which Is the Better Oxidant? *J. Phys. Chem. A* **2009**, *113*, 11635–11642.

7 Watanabe, Y.; Iyanagi, T.; Oae, S. Kinetic Study on Enzymatic S-Oxygenation Promoted by a Reconstituted System with Purified Cytochrome P-450. *Tetrahedron Lett.* **1980**, *21*, 3685–3688.

8 Baciocchi, E.; Lanzalunga, O.; Pirozzi, B. Oxidation of Benzyl and Phenethyl Sulfides. Implications on the Mechanism of the Microsomal and Biomimetic Oxidation of Sulfides. *Tetrahedron* **2004**, *53*, 12287–12298.

9 Bathelt, C. M.; Ridder, L.; Mulholland, A. J.; Harvey, J. N. Mechanism and Structure-Reactivity Relationships for Aromatic Hydroxylation by Cytochrome P450. *Org. Biomol. Chem.* **2004**, *2*, 2998–3005.

10 Shaik, S. S. What Happens to Molecules as They React? A Valence Bond Approach to Reactivity. *J. Am. Chem. Soc.* **1981**, *103*, 3692–3701.

11 Shaik, S.; Shurki, A. Valence Bond Diagrams and Chemical Reactivity. *Angew. Chem., Int. Ed.* **1999**, *38*, 586–625.

12 Shaik, S.; Hiberty, P. C. *A Chemist's Guide to Valence Bond Theory*; John Wiley & Sons: Hoboken, NJ, 2008.

13 Shaik, S.; Cohen, S.; de Visser, S. P.; Sharma, P. K.; Kumar, D.; Kozuch, S.; Ogliaro, F.; Danovich, D. The "Rebound Controversy": An Overview and Theoretical Modeling of the Rebound Step in C−H Hydroxylation by Cytochrome P450. *Eur. J. Inorg. Chem.* **2004**, 207–226.

14 Shaik, S.; Kumar, D.; de Visser, S. P. A Valence Bond Modeling of Trends in Hydrogen Abstraction Barriers and Transition States of Hydroxylation Reactions Catalyzed by Cytochrome P450 Enzymes *J. Am. Chem. Soc.* **2008**, *130*, 10128−10140; *130*, 14016 (Correction).

15 Latifi, R.; Bagherzadeh, M.; de Visser, S. P. Origin of the Correlation of the Rate Constant of Substrate Hydroxylation by Nonheme Iron(IV)-oxo Complexes with the Bond-Dissociation Energy of the C−H Bond of the Substrate. *Chem.—Eur. J.* **2009**, *15*, 6651–6662.

16 Kang, Y.; Chen, H.; Jeong, Y. J.; Lai, W.; Bae, E. H.; Shaik, S.; Nam, W. Enhanced Reactivities of Iron(IV)-Oxo Porphyrin π-Cation Radicals in Oxygenation Reactions by Electron-Donating Axial Ligands. *Chem.—Eur. J.* **2009**, *15*, 10039–10046.

17 Shaik, S.; Filatov, M.; Schröder, D.; Schwarz, H. Electronic Structure Makes a Difference: Cytochrome P-450 Mediated Hydroxylations of Hydrocarbons as a Two-State Reactivity Paradigm. *Chem.—Eur. J.* **1998**, *4*, 193–199.

18 Carter, E. A.; Goddard, W. A., III. Early- Versus Late-Transition-Metal-Oxo Bonds: The Electronic Structure of VO^+ and RuO^+. *J. Phys. Chem.* **1988**, *92*, 2109–2115.

19 Su, P.; Song, L.; Wu, W.; Hiberty, P. C.; Shaik, S. Valence Bond Calculations of Hydrogen Transfer Reactions: A General Predictive Pattern Derived from Theory. *J. Am. Chem. Soc.* **2004**, *126*, 13539–13549.

20 (a) Bell, R. P. The Theory of Reactions Involving Proton Transfers. *Proc. R. Soc. London, Ser. A* **1936**, *154*, 414–429. (b) Evans, M. G.; Polanyi, M. Inertia and Driving Force of Chemical Reactions. *Trans. Faraday Soc.* **1938**, *34*, 11–24.

21 The $\pi^* \rightarrow a_{2u}$ promotion in Ψ_I^*(IV) involves 5−6 kcal/mol.

22 (a) de Visser, S. P.; Kumar, D.; Cohen, S.; Shacham, R.; Shaik, S. A Predictive Pattern of Computed Barriers for C−H hydroxylation by Compound I of Cytochrome

P450. *J. Am. Chem. Soc.* **2004**, *126*, 8362–8363. (b) Olsen, L.; Rydberg, P.; Rod, T. H.; Ryde, U. Prediction of Activation Energies for Hydrogen Abstraction by Cytochrome P450. *J. Med. Chem.* **2006**, *49*, 6489–6499. (c) Wang, Y.; Kumar, D.; Yang, C.; Wang, H.; Han, K.; Shaik, S. Theoretical Study of *N*-Demethylation of Substituted *N,N*-dimethylanilines by Cytochrome P450: The Mechanistic Significance of Kinetic Isotope Effect Profiles. *J. Phys. Chem. B* **2007**, *111*, 7700–7710.

23 Sanderson, R. T. *Polar Covalence*; Academic Press: New York, 1983.

24 Newcomb, M.; Toy, P. H. Hypersensitive Radical Probes and the Mechanisms of Cytochrome P450-Catalyzed Hydroxylation Reactions. *Acc. Chem. Res.* **2000**, *33*, 449–455.

25 Kumar, D.; de Visser, S. P.; Sharma, P. K.; Cohen, S.; Shaik, S. Radical Clock Substrates, Their C−H Hydroxylation Mechanism by Cytochrome P450, and Other Reactivity Patterns: What Does Theory Reveal about the Clocks' Behavior? *J. Am. Chem. Soc.* **2004**, *126*, 1907–1920.

26 Sharma, P. K.; de Visser, S. P.; Ogliaro, F.; Shaik, S. Is the Ruthenium Analogue of Compound I of Cytochrome P450 an Efficient Oxidant? A Theoretical Investigation of the Methane Hydroxylation Reaction. *J. Am. Chem. Soc.* **2003**, *125*, 2291–2300.

27 Song, L.; Wu, W.; Hiberty, P. C.; Shaik, S. Identity S_N2 Reactions $X^- + CH_3X \rightarrow XCH_3 + X^-$ (X = F, Cl, Br, and I) in Vacuum and Aqueous Solution: A Valence Bond Study. *Chem.—Eur. J.* **2006**, *12*, 7458–7466.

28 Shaik, S. S. Nucleophilicity and Vertical Ionization Potentials in Cation−Anion Recombinations. *J. Org. Chem.* **1987**, *52*, 1563–1568.

29 Goto, Y.; Matsui, T.; Ozaki, S.; Watanabe, Y.; Fukuzumi, S. Mechanisms of Sulfoxidation Catalyzed by High-Valent Intermediates of Heme Enzymes: Electron-Transfer vs Oxygen-Transfer Mechanism. *J. Am. Chem. Soc.* **1999**, *121*, 9497–9502.

30 Mayer, J. M. Hydrogen Atom Abstraction by Metal-Oxo Complexes: Understanding the Analogy with Organic Radical Reactions. *Acc. Chem. Res.* **1998**, *31*, 441–450.

31 Decker, A.; Rohde, J.-U.; Klinker, E. J.; Wong, S. D.; Que, L., Jr.; Solomon, E. I. Spectroscopic and Quantum Chemical Studies on Low-Spin Fe^{IV}═O Complexes: Fe−O Bonding and Its Contributions to Reactivity. *J. Am. Chem. Soc.* **2007**, *129*, 15983–15996.

32 Kaizer, J.; Klinker, E. J.; Oh, N. Y.; Rohde, J.-U.; Song, W. J.; Stubna, A.; Kim, J.; Münck, E.; Nam, W.; Que, L., Jr. Nonheme $Fe^{IV}O$ Complexes That Can Oxidize the C−H Bonds of Cyclohexane at Room Temperature. *J. Am. Chem. Soc.* **2004**, *126*, 472–473.

33 Gupta, R.; Borovik, A. S. Monomeric $Mn^{III/II}$ and $Fe^{III/II}$ Complexes with Terminal Hydroxo and Oxo Ligands: Probing Reactivity via O−H Bond Dissociation Energies. *J. Am. Chem. Soc.* **2003**, *125*, 13234–13242.

34 (a) Song, W. J.; Ryu, Y. O.; Song, R.; Nam, W. Oxoiron(IV) Porphyrin π-Cation Radical Complexes with a Chameleon Behavior in Cytochrome P450 Model Reactions. *J. Biol. Inorg. Chem.* **2005**, *10*, 294–304. (b) Takahashi, A.; Kurahashi, T.; Fujii, H. Effect of Imidazole and Phenolate Axial Ligands on the Electronic Stucture and Reactivity of Oxoiron(IV) Porphyrin π-Cation Radical Complexes: Drastic Increase in Oxo-Transfer and Hydrogen Abstraction Reactivities. *Inorg. Chem.* **2009**, *48*, 2614–2625. (c) de Visser, S. P. The Axial Ligand Effect of Oxo-Iron Porphyrin Catalysts. How Does Chloride Compare to Thiolate? *J. Biol. Inorg. Chem.* **2006**, *11*, 168–178. (d) Kamachi, T.; Kouno, T.; Nam, W.; Yoshizawa, K. How Axial Ligands Control the Reactivity of High-Valent Iron(IV)-Oxo Porphyrin π-Cation Radicals in Alkane Hydroxylation: A Computational Study. *J. Inorg. Biochem.* **2006**, *100*, 751–754.

35 de Visser, S. P. Trends in Substrate Hydroxylation Reaction by Heme and Nonheme Iron(IV)-Oxo Oxidants Give Correlations between Intrinsic Properties of the Oxidant with Barrier Height. *J. Am. Chem. Soc.* **2010**, *132*, 1087–1097.

36 Computed herein.

37 (a) Que, L., Jr. The Road to Non-Heme Oxoferryls and Beyond. *Acc. Chem. Res.* **2007**, *40*, 493–500. (b) Nam, W. High-Valent Iron(IV)-Oxo Complexes of Heme and Non-Heme Ligands in Oxygenation Reactions. *Acc. Chem. Res.* **2007**, *40*, 522–531.

38 (a) Kumar, D.; Hirao, H.; Que, L., Jr.; Shaik, S. Theoretical Investigation of C-H Hydroxylation by $(N4Py)Fe^{IV}$═O^{2+}: An Oxidant More Powerful than P450. *J. Am. Chem. Soc.* **2005**, *127*, 8026–8027. (b) Johansson, A. J.; Blomberg, M. R. A.; Siegbahn, P. E. M. Quantum Chemical Modeling of the Oxidation of Dihydroanthracene by the Biomimetic Nonheme Iron Catalyst $[(TMC)Fe^{IV}(O)]^{2+}$. *J. Phys. Chem. C* **2007**, *111*, 12397–12406. (c) Bernasconi, L.; Louwerse, M. J.; Baerends, E. J. The Role of Equatorial and Axial Ligands in Promoting the Activity of Non-Heme Oxidoiron(IV) Catalysts in Alkane Hydroxylation. *Eur. J. Inorg. Chem.* **2007**, 3023–3033. (d) de Visser, S. P. Propene Activation by the Oxo-Iron Active Species of Taurine/α-Ketoglutarate Dioxygenase (TauD) Enzyme. How Does the Catalysis Compare to Heme-Enzymes? *J. Am. Chem. Soc.* **2006**, *128*, 9813–9824.

39 Balcells, D.; Raynaud, C.; Crabtree, R. H.; Eisenstein, O. A Rational Basis for the Axial Ligand Effect in C-H Oxidation by $[MnO(porphyrin)(X)]^+$ (X = H_2O, OH^-, O^{2-}) from a DFT Study. *Inorg. Chem.* **2008**, *128*, 10090–10099.